

pubsiacs.org/Nanol ett Letter

Boosting Inversion Symmetry Breaking in Epitaxial Tetragonal ZrO₂ Via Atomic Layer Deposition

Jung Woo Cho, ◆ Dongmin Kim, ◆ In Hyeok Choi, R. A. Madusanka Pushpakumara, Sungsu Kang, Tae Yoon Lee, Chihwan An, Seung Hyup Lee, Jong Seok Lee, Jungwon Park,* and Seung Chul Chae*



Cite This: Nano Lett. 2025, 25, 11673-11679



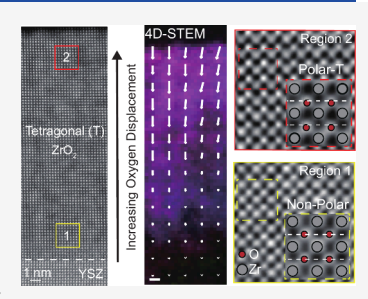
ACCESS I

Metrics & More

Article Recommendations

Supporting Information

ABSTRACT: The stabilization of intermediate polar phases in fluorite-structured oxides is critical for advancing ferroelectric and antiferroelectric applications. Here, we report the stabilization of epitaxial polar tetragonal (T) ZrO_2 . Epitaxial $Hf_xZr_{1-x}O_2$ thin films (x = 1, 0.75, 0.5, 0.25, and 0) are synthesized on (001) yttria-stabilized zirconia substrates via atomic layer deposition. The emergence of the unprecedented polar T-ZrO₂ phase deviates from the expected phase transition from nonpolar HfO₂ through ferroelectric Hf_{0.5}Zr_{0.5}O₂ to antiferroelectric Zrrich Hf_xZr_{1-x}O₂. Second harmonic generation measurements reveal unexpected inversion symmetry breaking in T-phase ZrO₂. High-resolution 4D-scanning transmission electron microscopy further confirms the presence of electric dipoles originating from off-centered oxygen displacements. These findings establish a pathway for the low-temperature epitaxial synthesis of HfO₂-ZrO₂-based materials and provide critical insight into the polar nature of T-phase ZrO₂.



KEYWORDS: Epitaxial growth, Atomic layer deposition, HfO2, ZrO2, 4D-STEM

he discovery of (anti)ferroelectricity in fluorite structure [Hf/Zr]O₂-based thin films has attracted significant interest due to their compatibility with complementary metal-oxide semiconductor (CMOS) technology. 1-3 In particular, the robust scalability of ferroelectricity in 1 nmthick HfO₂ has been attributed to the presence of flat phonon band.^{4,5} These properties have enabled the integration of [Hf/ Zr]O₂-based materials into next-generation devices such as ferroelectric field-effect transistor (FeFETs) and artificial synapses.^{3,6} Antiferroelectric phases, on the other hand, have been widely studied for energy storage applications due to their large energy density and high breakdown strength.⁷ Epitaxial HfO₂-based thin films have provided a model platform to investigate phase stabilization mechanisms, where strain engineering have been effectively used to induce noncentrosymmetric phases such as rhombohedral (R-, R3m) and orthorhombic (O-, Pca21), enhancing ferroelectric performance.8-11 While significant progress has been made in understanding and controlling the ferroelectric properties of HfO₂, comparatively fewer studies have focused on pure ZrO₂, despite its structural similarity within the fluorite family.

Unlike HfO2, ZrO2 thin films predominantly stabilize into the tetragonal phase (T-, P42/nmc) at similar thickness scales (~10 nm). ^{13,14} In this T-phase, ZrO₂ typically exhibits antiferroelectric behavior. 15 Polycrystalline ZrO2 films deposited by atomic layer deposition (ALD) generally crystallize into the T-phase and display antiferroelectric characteristics. 16,17 However, recent studies have demonstrated that ferroelectric O-phase can be induced even in ultrathin ZrO2 films down to a few unit-cell thickness, as confirmed by second harmonic generation (SHG) measurements and transmission electron microscopy (TEM) oxygen imaging. 18 In addition, pulsed laser deposition (PLD) has enabled the growth of epitaxial ZrO2 thin films, where ferroelectricity has been observed not only in the conventionally reported R- and O- phase, but also in the Tphase. 19-21 These findings highlight the possibility of accessing ferroelectricity in pure ZrO2 through careful phase engineering, emphasizing the crucial role of deposition conditions and strain in stabilizing polar phases.

Recently, epitaxial growth of Hf_{0.5}Zr_{0.5}O₂ (HZO) thin films by ALD has been demonstrated, enabling the synthesis of high quality epitaxial films with precise compositional control.²² Building upon this achievement, in this study, epitaxial Hf_xZr_{1-x}O₂ thin films were fabricated across the various Zr concentrations to systematically investigate the phase evolution from HfO2 to ZrO2. The structure of HfxZr1-xO2 thin films was investigated by X-ray diffraction (XRD) and scanning transmission electron microscopy (STEM). In particular, polar T-phase was demonstrated in pure ZrO₂ thin films, beyond the conventionally reported nonpolar T-phase. Oxygen sublattice distortion enables the stabilization of a polar T-phase in ZrO₂ revealing a novel phase for realizing ferroelectricity beyond the conventional O-, and R-phases.

Received: May 22, 2025 Revised: July 14, 2025 Accepted: July 15, 2025 Published: July 18, 2025





Nano Letters pubs.acs.org/NanoLett Letter

Epitaxial $Hf_xZr_{1-x}O_2$ thin films with varying Zr concentrations were fabricated on YSZ (001) substrates via ALD. YSZ single-crystalline substrates were employed for thin film growth due to their excellent lattice matching with HfO_2 -based polymorphs, introducing a biaxial strain ranging from -3.03% to +1.79% (Table S1). Figure 1a shows the XRD $\theta - 2\theta$

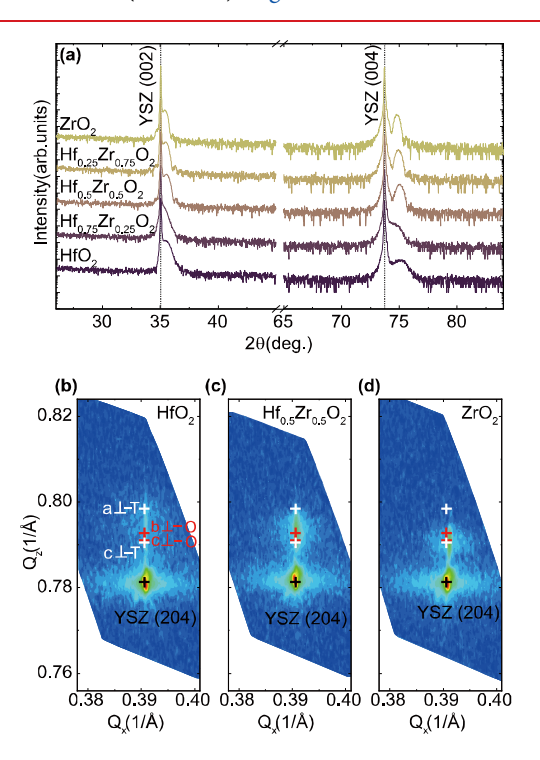


Figure 1. Epitaxial growth of $Hf_xZr_{1-x}O_2$ thin films on YSZ substrate. (a) θ - 2θ XRD patterns of epitaxial $Hf_xZr_{1-x}O_2$ thin films with various Zr concentration (x = 0, 0.25, 0.5, 0.75, and 1) on the YSZ (001) substrate. (b-d) X-ray reciprocal space mapping (RSM) of $Hf_xZr_{1-x}O_2$ films with x values (b) 1, (c) 0.5, and (d) 0 at (204) reflections, respectively.

patterns of the $Hf_xZr_{1-x}O_2$ films with Hf/Zr compositions of x = 1, 0.75, 0.5, 0.25, and 0 to confirm the epitaxial growth. The broad, rounded peaks observed at 2θ values between $35^{\circ}-36^{\circ}$ and 74°-76°, adjacent to the YSZ (002) and (004) diffraction peaks, were identified as the {002} and {004} planes of $Hf_xZr_{1-x}O_2$, respectively. Notably, the diffraction peaks for the $Hf_xZr_{1-x}O_2$ layer were only obtained within the 2θ ranges of $35^{\circ}-36^{\circ}$ and $74^{\circ}-76^{\circ}$, which indicates the formation of a single-phase structure. Cross-sectional high-angle annular darkfield scanning transmission electron microscopy (HAADF-STEM) images of the $Hf_xZr_{1-x}O_2$ thin films also show uniform deposition on the YSZ substrate with a clear interface and surface, which is consistent with the atomic force microscopy (AFM) results (Figures S1 and S2). Compositional analysis using TEM-energy dispersive spectroscopy (EDS) confirmed that the Hf/Zr ratios of the films were systematically controlled in five increments, from HfO_2 (x = 1) to ZrO_2 (x = 0) and closely matched the target compositions (Figure S1).

A strong lattice coherence between the $Hf_xZr_{1-x}O_2$ thin film and the YSZ substrate was conserved during the lowtemperature growth. X-ray reciprocal space mapping (RSM) was performed to verify the in-plane structural coherence between the Hf_xZr_{1-x}O₂ films and the YSZ substrate. Figure 1b-d presents the RSMs around the YSZ (204) diffraction peak for the Hf_xZr_{1-x}O₂ thin films with x values of 1, 0.5, and 0, respectively. Across all the compositions, distinct $Hf_xZr_{1-x}O_2$ peaks were observed at $Q_x \sim 0.390$ and $Q_z \sim$ 0.795, which indicates strong in-plane crystallinity and coherent alignment of the Hf_xZr_{1-x}O₂ films with the YSZ substrate. The white and red cross symbols represent the expected diffraction peaks corresponding to the T- and Ophases of the fully strained cases, respectively. In particular, for the O-phase, out-of-plane diffraction peaks of b- and coriented films can be obtained at $Q_z \sim 0.793$ and 0.791, respectively. For the T-phase, the out-of-plane diffraction peaks of a- and c- oriented films can appear at $Q_z \sim 0.798$ and 0.791, respectively. The monoclinic (M)-phase (a, b, and c = 5.11, 5.18, and 5.28, respectively; $\beta = 100.09^{\circ}$ in bulk)¹³ typically

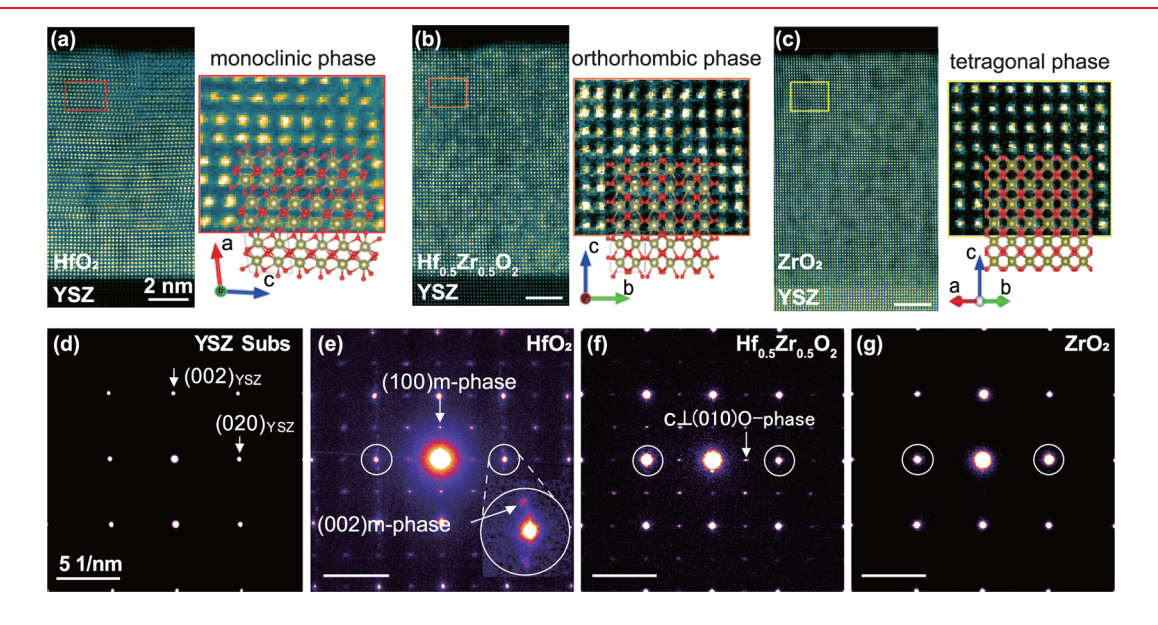


Figure 2. Cross-section TEM images of the $Hf_xZr_{1-x}O_2$ samples. (a-c) HAADF-STEM images for varying Zr concentrations, along with high-magnification images corresponding to the solid boxes in each image and the simulated crystal structures: (a) HfO_2 (x = 1), (b) $Hf_{0.5}Zr_{0.5}O_2$ (x = 0.5), (c) ZrO_2 (x = 0). (d-g) SAED patterns of the YSZ substrate and $Hf_xZr_{1-x}O_2$ thin films with x values of (e) x = 1, (f) x = 0.5, and (g) x = 0.

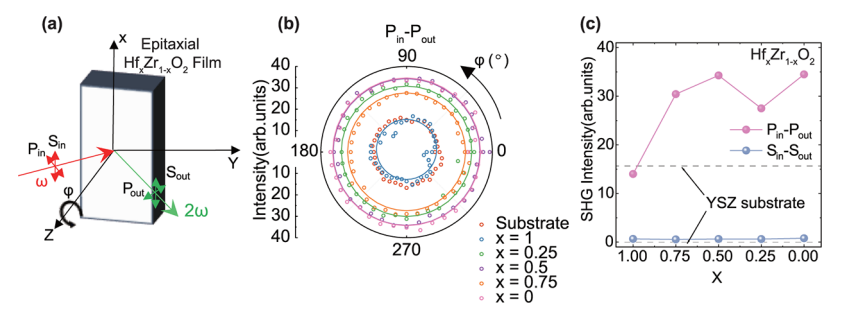


Figure 3. SHG measurement for investigating inversion symmetry breaking in epitaxial $Hf_xZr_{1-x}O_2$ thin films on the YSZ (001) substrate. (a) This setup illustrates the measurement of the azimuth (φ) dependency. The polarization states are identified as P_{in} and S_{in} for the fundamental wave, and P_{out} and S_{out} for the second-harmonic wave. (b) Representative azimuth (φ) -dependent SHG polar pattern in the P_{in} - P_{out} of the substrate and $Hf_xZr_{1-x}O_2$ (x = 0, 0.25, 0.5, 0.75, and 1) thin films. (c) Average intensity of the $Hf_xZr_{1-x}O_2$ thin films with P_{in} - P_{out} and S_{in} - S_{out} configuration.

exhibits a *c*-oriented peak near $2\theta \approx 34.3^\circ$ which was absence in our XRD $\theta - 2\theta$ scan data and the RSM data with lower Q_z values. However, for *a*-oriented M-phase, Ce-doped HfO₂ was previously reported on the YSZ (001) substrate, exhibiting a diffraction peak near $2\theta \approx 35.8^\circ$, which can be obtained near $Q_z \sim 0.798.^{23}$ Owing to the overlapping diffraction peaks resulting from the fully strained state of the films, distinguishing individual phases in both XRD $\theta - 2\theta$ scans and RSM data remains challenging. Despite the difficulty in resolving individual diffraction peaks due to structural similarities among the $Hf_xZr_{1-x}O_2$ polymorphs, the RSM analysis demonstrated that high-quality epitaxial growth of the $Hf_xZr_{1-x}O_2$ films was obtained through ALD.

The epitaxial growth and systematic phase evolution from M-, O-, and finally to T-phase were directly observed in the $Hf_xZr_{1-x}O_2$ thin films with increasing Zr concentration. HAADF-STEM was performed to investigate the structural phase transitions in the Hf_xZr_{1-x}O₂ thin films with increasing Zr content. STEM images of $Hf_xZr_{1-x}O_2$ (x = 1, 0.5, and 0) are presented in Figure 2a-c, along with magnified images of the regions highlighted by the red, orange, and yellow solid-line boxes. The inverse fast Fourier transform (iFFT) images in Figure S3 show no additional planes (vertical lines) for all compositions, thereby indicating the absence of dislocations at the interface. The Hf atom arrangement in HfO_2 (x = 1) is in excellent agreement with the centrosymmetric M-phase, as indicated by the magnified red solid box region in Figure 2a. Similarly, a clear atom arrangement of the noncentrosymmetric O-phase along the (100) direction for the HZO (x = 0.5) thin film is seen in Figure 2b. In particular, for the HfO_2 (x = 1) thin film, HAADF-STEM analysis (Figure S4b) revealed that the film initially grows in a T-like structure due to epitaxial growth on the YSZ substrate. As the film becomes thicker, strain relaxation induces a phase transition into the more stable M-phase. Similarly, for the HZO (x = 0.5) thin film, a multiphase structure with partial coexistence of a T-like phase was also observed, as shown in Figure S4a. Lastly, in the case of the ZrO_2 (x = 0) thin films, the T-phase along the (110) direction is identified as shown in Figure 2c.

Phase formation in $Hf_xZr_{1-x}O_2$ thin films was further validated by selected area electron diffraction (SAED) patterns. For comparison, the SAED pattern of the pure YSZ substrate of the cubic crystal structure was confirmed with reflections corresponding to $(002)_{YSZ}$ and $(020)_{YSZ}$ as shown in Figure 2d. Figure 2e–g show the SAED patterns obtained from regions that encompass the areas shown in the high-resolution STEM images in Figure 2a–c, respectively. As indicated by the

arrows in Figure 2e and 2f for the interplanar diffraction peaks, the distinct structural diffraction patterns of the M- and Ophases were observed for the HfO_2 (x = 1) and HZO film (x = 0.5), respectively. Furthermore, for the HfO_2 film (x = 1), the diffraction peak associated with the M-phase with a β -angle of 99° was distinctly observed as shown in the magnified diffraction pattern with a large circle in Figure 2e, which confirms that the HfO_2 (x = 1) film was formed in the Mphase. For the HZO film (x = 0.5) as shown in Figure 2f, the (010) reflection of the O-phase was identified. On the other hand, Figure 2g (x = 0) shows the recovery of clear high symmetry diffraction patterns without interplanar diffraction peaks. Owing to the highly symmetric structure of the T-phase, the large interplanar spacings observed in the SAED patterns of the HfO_2 (x = 1) and HZO (x = 0.5) thin films were not observed.

Anomalous inversion symmetry breaking of ZrO2 was observed in the optical second harmonic response. To further investigate the structural symmetry of the Hf_xZr_{1-x}O₂ films, nonlinear optical second harmonic generation (SHG) experiments were performed, which sensitively revealed information about local inversion symmetry breaking. As illustrated in Figure 3a, the polarization of the fundamental wave was set to out-of-plane (P) or in-plane (S), denoted as P_{in} and S_{in} , respectively, with the corresponding second harmonic waves measured as P_{out} and S_{out} . Figure 3b presents the azimuth-(φ -)dependent SHG polar patterns of the substrate and $Hf_xZr_{1-x}O_2$ films in the P_{in} - P_{out} configuration, measured across different Zr concentrations (x = 1, 0.75, 0.5, 0.25, and 0). Figure 3c shows the SHG signals for both P_{in}-P_{out} and S_{in}-S_{out} in various Zr concentration. A strong SHG signal is detected in the P_{in}-P_{out} configuration, while the S_{in}-S_{out} configuration exhibits negligible intensity. This result suggests the absence of significant in-plane directional inversion symmetry breaking. However, the P_{in}-P_{out} signal intensity shows a clear dependence of Zr composition. For the HfO_2 (x = 1) film, the SHG intensity was nearly identical to that of the substrate, which indicates that the SHG signal from the film is negligible. This demonstrates that the HfO_2 (x = 1) film exhibited a centrosymmetric M-phase without any inversion symmetry breaking, which is consistent with our XRD results. However, films incorporating Zr up to x = 0.5 exhibited an increase in SHG intensity and reached the highest intensity in the HZO (x = 0.5) film as shown in Figure 3b. To our knowledge, in HfO₂-ZrO₂ systems, the SHG signals of Hf_xZr_{1-x}O₂ films cannot be obtained in the centrosymmetric T- and M- phases, but can emerge in the noncentrosymmetric O-phase.²⁴ As the

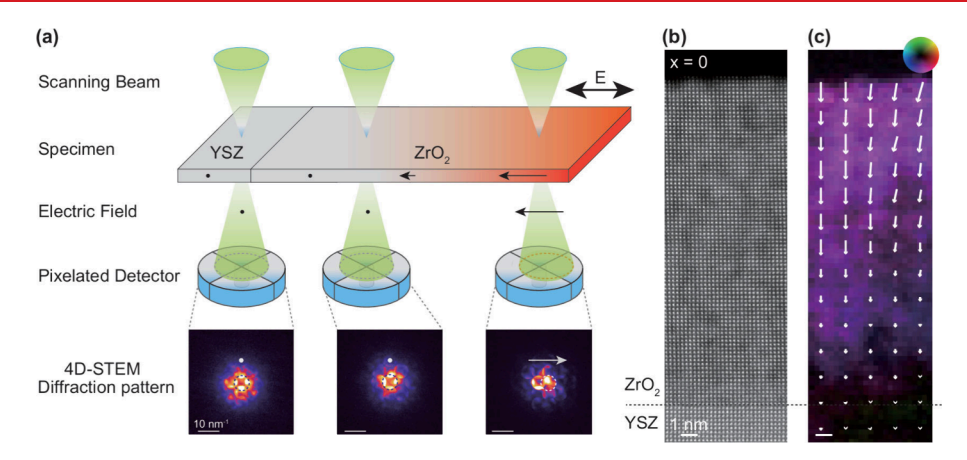


Figure 4. Investigating residual electric field in tetragonal ZrO₂ unit cell through 4D-STEM measurement. (a) 4D-STEM scheme for measuring electric field at epitaxial ZrO₂ thin film. The diffraction pattern at each position of the scanning electron beam is recorded using a pixelated detector, allowing for the measurement of the electric field within the thin films by calculating the center of mass (COM). (b) HAADF-STEM image of the ZrO₂ thin films epitaxially grown on a YSZ substrate. (c) 4D-STEM COM image corresponding to the region in (b), showing the direction and relative magnitude of electric field within the unit cell. The electric field directions are color-coded, with pixels of the same color indicating identical electric field direction.

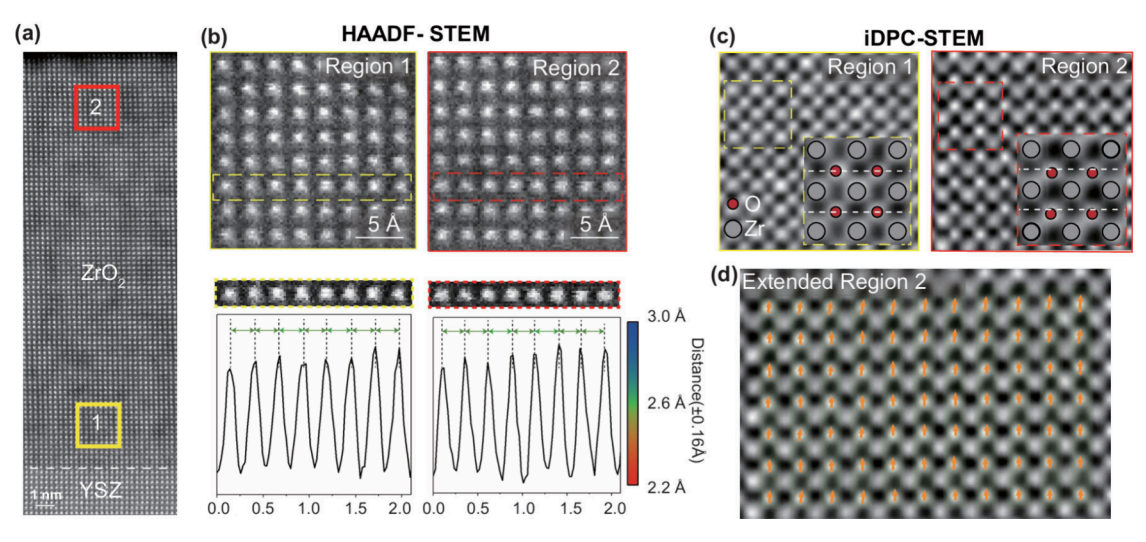


Figure 5. The observation of oxygen displacement in tetragonal ZrO_2 thin films. (a) HAADF-STEM image of the ZrO_2 (x=0) thin film. (b) High-resolution STEM images of the yellow and red regions highlighted in (a), with their corresponding atomic distances indicated as green arrows. (c) iDPC-STEM images of the areas marked by the solid yellow and red lines in (a). The yellow and red dashed line region shows a magnified image of the ZrO_2 unit cell. Zr is marked in the gray circle, and oxygen in the red circle. (d) The polarization map at red solid box region in (a). The dipole moment is polarized toward the top, as shown by the orange arrows. The arrow lengths are scaled by a factor of 3 to enhance the visibility of the displacement directions.

Zr ratio increases up to x=0.75, the SHG intensity decreased asymptotically, suggesting that the noncentrosymmetric structure partially recovered to the centrosymmetric structure. However, a pronounced re-enhancement of the SHG intensity was observed in the $\rm ZrO_2$ (x=0) film, while the crystal structure was confirmed to be in the T-phase through STEM analysis (Figure 2c and g).

Despite the global centrosymmetric nature of the T-phase ZrO₂, the presence of local broken inversion symmetry can be attributed to the potential appearance of additional local polar order of the ZrO₂ film. Similar SHG responses in structurally symmetric systems have been reported in other oxides and van der Waals materials, where subtle lattice distortions or interface-induced symmetry breaking give rise to noncentrosymmetric polar structures. For instance, Fe₃GeTe₂, a van der Waals topological ferromagnet, exhibits a robust SHG signal due to the transition from random defects to ordered Fe

vacancies.²⁵ Likewise, in compressively strained SrRuO₃ thin films, the asymmetric relaxation of the oxygen octahedral network was shown to induce a polar metallic phase with triclinic C₁ symmetry.²⁶ These findings suggest that even in high-symmetry phases like tetragonal ZrO₂, inversion symmetry breaking may emerge from local structural distortions, strain related oxygen distortion, or interfacial effects with the YSZ substrate. Furthermore, recent studies on oxide superlattices demonstrated that polar distortions can be stabilized and tuned by the coherently engineered layer thickness and strain,²⁷ implying that the observed SHG signal in our ZrO₂ thin films may similarly originate from hidden polar distortions at the atomic scale as discussed below.

The inhomogeneous distribution of electric field in the ZrO_2 thin films strengthened from the YSZ interface toward the surface. Figure 4a shows a schematic of the 4D-STEM technique and representative diffraction patterns. As the

nanoprobe beam scans across the specimen, it is scattered at various angles depending on the local electric field, and the resulting diffraction patterns are recorded by a pixelated detector. The electric field at each scan point is then extracted by analyzing the center of mass (COM) of the diffraction pattern. Due to the high sensitivity of this technique, 4D-STEM measurements can be affected by artifacts, particularly near the edges of TEM lamellae, where diffraction asymmetry may arise from thickness gradients, surface bending, or contamination. 28–30 These factors can distort the COM position and reduce the accuracy of electric field mapping. To mitigate such effects, specimens were carefully prepared using an optimized FIB milling protocol (Supporting Information, Experimental Methods), with uniform-thickness regions verified by STEM-EELS and diffraction analysis. As shown in Figure S5, these procedures effectively minimized preparation-induced artifacts. Figure 4b shows a cross-sectional HAADF-STEM image of the ZrO₂ film. By analyzing the COM of the scattered electron beam from the HAADF-STEM, the inhomogeneous local electric field is estimated as shown in Figure 4c. As depicted by the relatively small arrows in the YSZ substrate in Figure 4c, the cubic crystal structure of the YSZ substrate does not induce a residual electric field within its unit cell, resulting in no clear COM direction within the atomic resolution in the 4D-STEM analysis. Similarly, the ZrO2 thin film just above the YSZ substrate exhibited negligible COM distortion with little arrows indicating a nonpolar phase in the fully strained film. However, a gradual increase of the electric field of the ZrO₂ layer aligned perpendicularly to the YSZ substrate was observed with large arrows near the film surface, as shown in Figure 4c. Notably, the Zr atom alignment maintained a fully strained T-phase throughout the thin film, as indicated by the geometrical phase analysis results shown in Figure S6, which suggests that oxygen played a crucial role in the inversion symmetry breaking.

The enhanced electric field across the film can be attributed to the gradual increase in oxygen displacement within the Zr metal-oxygen framework. To elucidate the origin of the SHG signal and electric fields observed in the 4D-STEM results, detailed structural analyses of the ZrO2 film were conducted using HR-STEM and integrated differential phase contrast STEM (iDPC-STEM). Figure 5a and b shows the HR-STEM image of the ZrO2 and the magnified image of the nearinterface and surface regions, highlighted with yellow and red solid boxes, respectively. Figure 5b shows that all the atomic columns in the boxed region along the (110) zone axis of the T-phase were arranged at uniform intervals (green arrow). Additionally, the out-of-plane directional spacing of the near interface and surface region was also maintained as shown in Figure S7. The lattice parameters in both the in-plane and outof-plane directions, measured from the Zr atomic distances, are presented in Figure S8. Considering the spatial resolution limit of STEM analysis—on the order of several tens of picometers—the average values and standard deviations are reported. However, for the oxygen sublattice, the positions of oxygen atoms are noticeably displaced, providing key insight into the origin of the SHG signal in ZrO₂ thin films. The iDPC-STEM image in Figure 5c reveals that while the oxygen atom positions remain centered near the interface, they become shifted in the surface region. Consistent with the 4D-STEM results, the oxygen atoms become increasingly displaced toward the upper layers. The polarization map at region 2 (solid red box) is shown in Figure 5d, where the

arrows indicate the dipole moments associated with the displacement of oxygen atoms. Additionally, in the O-phase Hf/ZrO₂ films, repeating nonpolar and polar layers are observed, as shown in Figure S9. However, considering the shift of the oxygen atoms, ZrO₂ exhibits only polar layer regions. These findings demonstrate that the polar nature of the T-phase originates from the breaking of oxygen centrosymmetry, thereby providing an explanation for the SHG signal observed in the ZrO₂ thin films.

The emergence of the polar T-phase can be attributed to strain relaxation, with its reversible thermal stability further supporting its robust nature. Thickness and temperature dependent studies further corroborate the stability of the polar T-phase in ZrO2 thin films. A series of epitaxial ZrO2 films with varying thickness (7, 11, 15, 18, and 22 nm) were synthesized on YSZ (001) substrates under identical growth conditions. X-ray diffraction θ - 2θ scans confirmed epitaxial growth across all thicknesses, as indicated by the presence of sharp diffraction peaks adjacent to the YSZ (002) substrate reflection (Figure S10). SHG measurements revealed negligible signal from the 7 nm film, suggesting minimal polar distortion at this thickness. In contrast, SHG intensity increased progressively with thickness, reaching a maximum at 22 nm. This trend is consistent with previous 4D-STEM and iDPC-STEM analyses, which showed enhanced oxygen displacement away from the interface. Furthermore, temperature-dependent STEM studies revealed a reversible phase transition from the polar T-phase to M-phase upon heating to 573 K, and re-emergence of the T-phase upon cooling to room temperature, as shown in Figure S11. These findings collectively underscore the robust nature of the polar Tphase in epitaxial ZrO2 thin films. The origin of oxygen displacement and associated robust polar ordering require further investigation.

In summary, an unprecedented polar phase was observed in epitaxial T-phase $\rm ZrO_2$ thin films grown on YSZ (001) substrates via atomic layer deposition. Epitaxial $\rm Hf_xZr_{1-x}O_2$ films with varying Zr content exhibited a systematic phase transition from M- and O-phase to T-phase, as confirmed by XRD and STEM. SHG measurements revealed structural inversion symmetry breaking, with a notable SHG response even in the nominally centrosymmetric T-phase. 4D-STEM further revealed an internal electric field that strengthens from the interface toward the surface, attributed to oxygen displacement within the lattice. These findings underscore the critical role of composition in controlling phase structure and symmetry, offering pathways for integrating functional oxides into next-generation electronic devices.

ASSOCIATED CONTENT

Supporting Information

The Supporting Information is available free of charge at https://pubs.acs.org/doi/10.1021/acs.nanolett.5c02741.

Experimental methods, elemental composition values of Hf and Zr, atomic force microscopy, iFFT image, geometrical phase analysis, in-plane and out-of-plane directional atomic distance analysis of ZrO₂, and orthorhombic HZO structure, thickness dependence XRD and SHG results, temperature dependence STEM (PDF)

Nano Letters pubs.acs.org/NanoLett Letter

AUTHOR INFORMATION

Corresponding Authors

Jungwon Park — School of Chemical and Biological
Engineering, Institute of Chemical Process and Institute of
Engineering Research, College of Engineering, Seoul National
University, Seoul 08826, Republic of Korea; Center for
Nanoparticle Research, Institute for Basic Science (IBS),
Seoul 08826, Republic of Korea; Advanced Institute of
Convergence Technology, Seoul National University, Suwonsi, Gyeonggi-do 16229, Republic of Korea; ◎ orcid.org/
0000-0003-2927-4331; Email: jungwonpark@snu.ac.kr

Seung Chul Chae — Department of Physics Education and Center for Education Research, Seoul National University, Seoul 08826, Republic of Korea; orcid.org/0000-0002-0913-027X; Email: scchae@snu.ac.kr

Authors

Jung Woo Cho — Department of Physics Education, Seoul National University, Seoul 08826, Republic of Korea; orcid.org/0000-0002-2878-3209

Dongmin Kim — School of Chemical and Biological Engineering, Institute of Chemical Process, Seoul National University, Seoul 08826, Republic of Korea; Center for Nanoparticle Research, Institute for Basic Science (IBS), Seoul 08826, Republic of Korea; Samsung Advanced Institute of Technology, Samsung Electronics, Suwon-si, Gyeonggi-do 16678, Republic of Korea

In Hyeok Choi – Department of Physics and Photon Science, Gwangju Institute of Science and Technology (GIST), Gwangju 61005, Republic of Korea

R. A. Madusanka Pushpakumara — Department of Physics and Photon Science, Gwangju Institute of Science and Technology (GIST), Gwangju 61005, Republic of Korea

Sungsu Kang — School of Chemical and Biological Engineering, Institute of Chemical Process, Seoul National University, Seoul 08826, Republic of Korea; Center for Nanoparticle Research, Institute for Basic Science (IBS), Seoul 08826, Republic of Korea

Tae Yoon Lee — Department of Physics Education, Seoul National University, Seoul 08826, Republic of Korea; orcid.org/0000-0003-1754-8657

Chihwan An – Department of Physics Education, Seoul National University, Seoul 08826, Republic of Korea

Seung Hyup Lee – Department of Physics Education, Seoul National University, Seoul 08826, Republic of Korea; orcid.org/0009-0004-4732-7737

Jong Seok Lee – Department of Physics and Photon Science, Gwangju Institute of Science and Technology (GIST), Gwangju 61005, Republic of Korea; orcid.org/0000-0001-6317-7944

Complete contact information is available at: https://pubs.acs.org/10.1021/acs.nanolett.5c02741

Author Contributions

◆J.W.C. and D.K. contributed equally to this paper Notes

The authors declare no competing financial interest.

ACKNOWLEDGMENTS

This work was supported by the National Research Foundation of Korea (NRF) grant funded by the Korean Government (MSIT, NRF-2021R1A2C1094795, and NRF-

RS-2024-00444182) (J.W.C., T.Y.L., S.H.L., C.A., and S.C.C.). This research was also supported by the 'Center for Science Education in the Infosphere' funded by the four-stage BK21 (J.W.C.). This work was supported by the Institute for Basic Science (IBS-R006-D1), the National Research Foundation of Korea (NRF) grants funded by the Korean government (Ministry of Science and ICT) (Nos. RS-2024-00449965 and RS-2024-00421181) (D.K., S.K., and J.P.). This work was also supported by the National Research Foundation of Korea (NRF) grant funded by the Korea government (MSIT) (No. 2022R1A2C2007847) (J.S.L., I.H.C., and R.A.M.P.).

REFERENCES

- (1) Böscke, T. S.; Müller, J.; Bräuhaus, D.; Schröder, U.; Böttger, U. Ferroelectricity in hafnium oxide thin films. *Appl. Phys. Lett.* **2011**, 99 (10), No. 102903.
- (2) Park, M. H.; Lee, Y. H.; Kim, H. J.; Kim, Y. J.; Moon, T.; Kim, K. D.; Müller, J.; Kersch, A.; Schroeder, U.; Mikolajick, T.; Hwang, C. S. Ferroelectricity and Antiferroelectricity of Doped Thin HfO2-Based Films 2015, 27 (11), 1811–1831.
- (3) Böscke, T. S.; Müller, J.; Bräuhaus, D.; Schröder, U.; Böttger, U. Ferroelectricity in hafnium oxide: CMOS compatible ferroelectric field effect transistors. In 2011 International Electron Devices Meeting, 5–7 Dec. 2011; IEEE, 2011; pp 24.5.1–24.5.4. DOI: 10.1109/IEDM.2011.6131606
- (4) Cheema, S. S.; Kwon, D.; Shanker, N.; dos Reis, R.; Hsu, S.-L.; Xiao, J.; Zhang, H.; Wagner, R.; Datar, A.; McCarter, M. R.; Serrao, C. R.; Yadav, A. K.; Karbasian, G.; Hsu, C.-H.; Tan, A. J.; Wang, L.-C.; Thakare, V.; Zhang, X.; Mehta, A.; Karapetrova, E.; Chopdekar, R. V.; Shafer, P.; Arenholz, E.; Hu, C.; Proksch, R.; Ramesh, R.; Ciston, J.; Salahuddin, S. Enhanced ferroelectricity in ultrathin films grown directly on silicon. *Nature* **2020**, *580* (7804), 478–482.
- (5) Lee, H.-J.; Lee, M.; Lee, K.; Jo, J.; Yang, H.; Kim, Y.; Chae, S. C.; Waghmare, U.; Lee, J. H. Scale-free ferroelectricity induced by flat phonon bands in HfO₂. *Science* **2020**, *369* (6509), 1343–1347.
- (6) Mulaosmanovic, H.; Ocker, J.; Müller, S.; Noack, M.; Müller, J.; Polakowski, P.; Mikolajick, T.; Slesazeck, S. Novel ferroelectric FET based synapse for neuromorphic systems. In 2017 Symposium on VLSI Technology, 5–8 June 2017; IEEE, 2017; pp T176–T177. DOI: 10.23919/VLSIT.2017.7998165
- (7) Pešić, M.; Hoffmann, M.; Richter, C.; Mikolajick, T.; Schroeder, U. Nonvolatile Random Access Memory and Energy Storage Based on Antiferroelectric Like Hysteresis in ZrO2. *Adv. Funct. Mater.* **2016**, 26 (41), 7486–7494.
- (8) Wei, Y.; Nukala, P.; Salverda, M.; Matzen, S.; Zhao, H. J.; Momand, J.; Everhardt, A. S.; Agnus, G.; Blake, G. R.; Lecoeur, P.; Kooi, B. J.; Íñiguez, J.; Dkhil, B.; Noheda, B. A rhombohedral ferroelectric phase in epitaxially strained $Hf_{0.5}Zr_{0.5}O_2$ thin films. *Nat. Mater.* **2018**, *17* (12), 1095–1100.
- (9) Suzuki, T.; Shimizu, T.; Mimura, T.; Uchida, H.; Funakubo, H. Epitaxial ferroelectric Y-doped HfO₂ film grown by the RF magnetron sputtering. *Jpn. J. Appl. Phys.* **2018**, *57* (11S), No. 11UF15.
- (10) Shimizu, T.; Katayama, K.; Kiguchi, T.; Akama, A.; Konno, T. J.; Funakubo, H. Growth of epitaxial orthorhombic YO_{1.5}-substituted HfO₂ thin film. *Appl. Phys. Lett.* **2015**, *107* (3), No. 032910.
- (11) Shiraishi, T.; Choi, S.; Kiguchi, T.; Konno, T. J. Structural evolution of epitaxial CeO₂-HfO₂ thin films using atomic-scale observation: Formation of ferroelectric phase and domain structure. *Acta Mater.* **2022**, 235, No. 118091.
- (12) Li, X.; Xu, Z.; Hu, S.; Gu, M.; Zhu, Y.; Liu, Q.; Yang, Y.; Ye, M.; Li, J.; Chen, L. Ferroelectricity in Orthorhombic Zirconia Thin Films. *Nano Lett.* **2025**, *25* (11), 4220–4226.
- (13) Materlik, R.; Künneth, C.; Kersch, A. The origin of ferroelectricity in $Hf_{1-x}Zr_xO_2$: A computational investigation and a surface energy model. *J. Appl. Phys.* **2015**, *117* (13), No. 134109.
- (14) Mimura, T.; Shimizu, T.; Sakata, O.; Funakubo, H. Thickness dependence of phase stability in epitaxial Hf_xZr_{1-x}O₂ films. *Phys. Rev. Mater.* **2021**, 5 (11), No. 114407.

Nano Letters pubs.acs.org/NanoLett Letter

- (15) Müller, J.; Böscke, T. S.; Schröder, U.; Mueller, S.; Bräuhaus, D.; Böttger, U.; Frey, L.; Mikolajick, T. Ferroelectricity in Simple Binary ZrO₂ and HfO₂. *Nano Lett.* **2012**, *12* (8), 4318–4323.
- (16) Lee, S. H.; Lee, T. Y.; Lim, H. H.; Cho, J. W.; An, C.; Chae, S. C. Symmetry Engineering in Antiferroelectric ZrO₂ Thin Films via Split-Up Behavior. *ACS Appl. Electron. Mater.* **2025**, 7 (5), 2146–2152.
- (17) Song, M. S.; Park, K.; Lee, K.; Cho, J. W.; Lee, T. Y.; Park, J.; Chae, S. C. Selective Crystallization of Ferroelectric $Hf_xZr_{1-x}O_2$ via Excimer Laser Annealing. ACS Appl. Electron. Mater. 2023, 5 (1), 117–122
- (18) Cheema, S. S.; Shanker, N.; Hsu, S.-L.; Rho, Y.; Hsu, C.-H.; Stoica, V. A.; Zhang, Z.; Freeland, J. W.; Shafer, P.; Grigoropoulos, C. P.; Ciston, J.; Salahuddin, S. Emergent ferroelectricity in subnanometer binary oxide films on silicon. *Science* **2022**, *376* (6593), 648–652.
- (19) Silva, J. P. B.; Negrea, R. F.; Istrate, M. C.; Dutta, S.; Aramberri, H.; Iñiguez, J.; Figueiras, F. G.; Ghica, C.; Sekhar, K. C.; Kholkin, A. L. Wake-up Free Ferroelectric Rhombohedral Phase in Epitaxially Strained ZrO₂ Thin Films. *ACS Appl. Mater. Interfaces* **2021**, *13* (43), 51383–51392.
- (20) El Boutaybi, A.; Maroutian, T.; Largeau, L.; Matzen, S.; Lecoeur, P. Stabilization of the epitaxial rhombohedral ferroelectric phase in ZrO_2 by surface energy. *Phys. Rev. Mater.* **2022**, 6 (7), No. 074406.
- (21) El Boutaybi, A.; Maroutian, T.; Largeau, L.; Findling, N.; Brubach, J.-B.; Cervasio, R.; Degezelle, A.; Matzen, S.; Vivien, L.; Roy, P.; Karamanis, P.; Rérat, M.; Lecoeur, P. Ferroelectricity in Epitaxial Tetragonal ZrO₂ Thin Films. *Adv. Electron. Mater.* **2024**, *10* (1), No. 2300516.
- (22) Cho, J. W.; Song, M. S.; Choi, I. H.; Go, K.-J.; Han, J.; Lee, T. Y.; An, C.; Choi, H.-J.; Sohn, C.; Park, M. H.; Baek, S.-H.; Lee, J. S.; Choi, S.-Y.; Chae, S. C. Atomic Layer Deposition of Epitaxial Ferroelectric $Hf_{0.5}Zr_{0.5}O_2$ Thin Films. *Adv. Funct. Mater.* **2024**, 34 (24), No. 2314396.
- (23) Shiraishi, T.; Choi, S.; Kiguchi, T.; Shimizu, T.; Funakubo, H.; Konno, T. J. Formation of the orthorhombic phase in CeO₂-HfO₂ solid solution epitaxial thin films and their ferroelectric properties. *Appl. Phys. Lett.* **2019**, *114* (23), No. 232902.
- (24) Ihlefeld, J. F.; Luk, T. S.; Smith, S. W.; Fields, S. S.; Jaszewski, S. T.; Hirt, D. M.; Riffe, W. T.; Bender, S.; Constantin, C.; Ayyasamy, M. V.; Balachandran, P. V.; Lu, P.; David Henry, M.; Davids, P. S. Compositional dependence of linear and nonlinear optical response in crystalline hafnium zirconium oxide thin films. *J. Appl. Phys.* **2020**, *128* (3), No. 034101.
- (25) Zhang, K.-X.; Ju, H.; Kim, H.; Cui, J.; Keum, J.; Park, J.-G.; Lee, J. S. Broken Inversion Symmetry in Van Der Waals Topological Ferromagnetic Metal Iron Germanium Telluride. *Adv. Mater.* **2024**, 36 (14), No. 2312824.
- (26) Roh, C. J.; Jung, M.-C.; Kim, J. R.; Go, K.-J.; Kim, J.; Oh, H. J.; Jo, Y.-R.; Shin, Y. J.; Choi, J. G.; Kim, B.-J.; Noh, D. Y.; Choi, S.-Y.; Noh, T. W.; Han, M. J.; Lee, J. S. Polar Metal Phase Induced by Oxygen Octahedral Network Relaxation in Oxide Thin Films. *Small* **2020**, *16* (40), No. 2003055.
- (27) Choi, I. H.; Jeong, S. G.; Jeong, D.-G.; Seo, A.; Choi, W. S.; Lee, J. S. Engineering the Coherent Phonon Transport in Polar Ferromagnetic Oxide Superlattices. *Adv. Sci.* **2025**, *12* (2), No. 2407382.
- (28) Ophus, C. Four-Dimensional Scanning Transmission Electron Microscopy (4D-STEM): From Scanning Nanodiffraction to Ptychography and Beyond. *Microsc. Microanal.* **2019**, 25 (3), 563–582.
- (29) Sadri, A.; Petersen, T. C.; Terzoudis-Lumsden, E. W. C.; Esser, B. D.; Etheridge, J.; Findlay, S. D. Unsupervised deep denoising for four-dimensional scanning transmission electron microscopy. *Npj Comput. Mater.* **2024**, *10* (1), 243.
- (30) da Silva, B. C.; Momtaz, Z. S.; Bruas, L.; Rouviére, J.-L.; Okuno, H.; Cooper, D.; den-Hertog, M. I., The influence of illumination conditions in the measurement of built-in electric field at p—n

junctions by 4D-STEM. Appl. Phys. Lett. 2022, 121 (12). DOI: 10.1063/5.0104861